Electronic Materials Letters (2023) 19:442–451
https://doi.org/10.1007/s13391-023-00423-6

ORIGINAL ARTICLE - ELECTRONICS, MAGNETICS AND PHOTONICS

Low Frequency Magnetoelectric Effect in $Bi_{0.5}Na_{0.5}TiO_3$–$Ni_{0.5}Zn_{0.5}Fe_2O_4$ Particulate Composites

Parminder Singh[1] · Radhapiyari Laishram[2] · Jayant Kolte[1] · Puneet Sharma[1]

Received: 14 December 2022 / Accepted: 23 February 2023 / Published online: 18 March 2023

Abstract

We report structural, dielectric, ferroelectric, magnetic, and low frequency magnetoelectric (*ME*) properties of $(1-x)$ $Bi_{0.5}Na_{0.5}TiO_3$ (BNT)–$xNi_{0.5}Zn_{0.5}Fe_2O_4$ (NZFO) (x = 0.05–0.30) microwave sintered particulate composites. Distinct phases of BNT and NZFO were confirmed by X-ray diffraction and scanning electron microscopy. Raman spectroscopy measurement showed the absence of micro-strains within the composite. The temperature dependent dielectric studies revealed the ferroelectric to anti-ferroelectric transition at 220 °C and anti-ferroelectric to paraelectric transition at 320 °C. The *ac* conductivity showed both frequency dependent and independent behavior. Temperature dependent *dc* conductivity showed that upto 200 °C charge conduction is due to hopping of electrons, whereas at higher temperature diffusion of oxygen vacancies are responsible for the conduction. Ferroelectric and leakage current density measurements showed enhanced conduction losses with NZFO content. The maximum *ME* coefficient at 10 Hz frequency is obtained for 0.80BNT–0.20NZFO (4.33 mV/cm.Oe at 800 Oe).

Graphical abstract

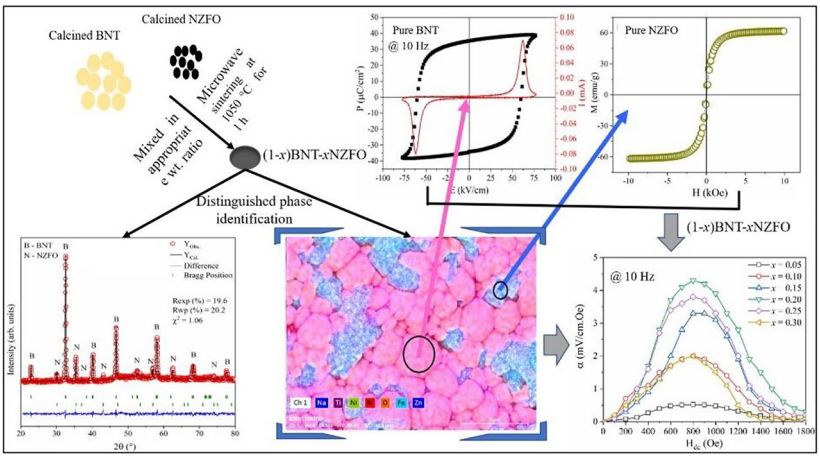

Keywords Composite materials · Ferroelectrics · Ferromagnetic · Magnetoelectric

✉ Puneet Sharma
puneet.sharma@thapar.edu

[1] School of Physics and Materials Science, Thapar Institute of Engineering and Technology, Patiala, Punjab 147004, India

[2] Solid State Physics Laboratory, Lucknow Road, Timarpur, Delhi 110054, India

1 Introduction

The magnetoelectric (*ME*) composites has gained great deal of attention over to single phase multiferroics due to its strain mediated *ME* coupling between piezoelectric and magnetostrictive phase [1–3]. Such *ME* composites with high coupling have paved the way for practical device application in meRAMs, sensors, and low frequency energy harvesters etc. [4–8]. The resultant *ME* coupling depends upon the type of magnetic and piezoelectric phase, their relative fraction, and type of geometry [9, 10]. Among the choices, Pb-based piezoelectric materials showed highest *ME* coupling due to its high piezoelectric coefficient (d_{33}), high remanent polarization (P_r) and low coercivity (E_c) [11, 12]. Several reports on Pb-based *ME* composites as energy harvesters evidences its enormous *ME* response [13–15]. However, the hazardous effect of Pb, inclined researchers to explore the environment friendly alternate piezoelectric phase with slightly compromised properties [16–19]. One of the most investigated piezoelectric phase is $Bi_{0.5}Na_{0.5}TiO_3$ (BNT) which possess good $P_r \sim 38$ μC cm^{-2}, moderate $d_{33} \sim 58$–95 pC/N and high temperature sustainability upto 320 °C [20–22]. On the other hand, spinel $NiFe_2O_4$ (NFO) is suitable magnetic phase as it exhibit strong piezomagnetic coefficient ($d\lambda/dH \sim 251$ ppm/T), good saturation magnetization ($M_s \sim 55$ emu/g) and low coercivity ($H_c \sim 180$ Oe) [23–25]. Further, the partial substitution of Ni^{2+} by Zn^{2+} enhances the M_S as well $d\lambda/dH$ [26–28].

Several studies on BNT based composites with different spinel ferrites were carried out and demonstrated the presence of *ME* coupling (4.0–7.5 mV/cm.Oe) [29–32]. However, the applied frequency and *dc* magnetic field was 1 kHz and 3–5 kOe respectively, which is relatively high for device realization. In this work, composites of BNT and $Ni_{0.5}Zn_{0.5}Fe_2O_4$ (NZFO) were prepared by microwave sintering and their structural, dielectric and *ME* properties were investigated. The *ME* coupling of 4.3 mV/cm.Oe at very low magnetic field (800 Oe) and frequency (10 Hz) is observed, which indicate this *ME* composite could be a potential material, where low frequency is prerequisite requirement.

2 Experimental

High purity $Bi(NO_3)_3$ $5H_2O$, CH_3COONa, $TiC_{12}H_{28}O_4$, $Fe(NO_3)_3$ $9H_2O$, $Ni(NO_3)_2$ $5H_2O$, and $Zn(NO_3)_2$ $6H_2O$, were used to synthesized BNT and NZFO powders. The respective phase precursors were weighed in stoichiometry ratio and dissolved in acetic acid, and 2-methoxy ethanol for preparing solution of BNT and in deionized water, and citric acid for synthesizing solution of NZFO. The pH for solution of NZFO was maintained at 7 by adding ammonia into it. These solutions were continuously stirred and set at 120 °C till the gel formation. The obtained gels were dried at 180 °C and a white powder was obtained for BNT whereas the combustion has taken place for NZFO. The as-synthesized powders of BNT and NZFO were calcined at 600 °C and 900 °C respectively for 3 h. To prepare $(1-x)$BNT–xNZFO composites ($x = 0.05$–0.30; $\Delta x = 0.05$), the appropriate weight ratio of calcined powders were wet mixed using planetary ball mill for 3 h. The rpm and charge to ball ratio were fixed to 250 and 1:5 respectively. After mixing, powders were dried and uniaxially pressed into cylindrical pellets at a pressure of 50 MPa. The sintering of as-pressed pellets were carried out in microwave furnace at 1050 °C for 1 h. The phase identification of sintered pellets were carried out by X-ray diffraction (XRD) (X'PERT Pro, PANalytical) pattern, using Cu–K_α radiation. Raman spectroscopy was carried out by Micro-Raman Spectrometer (Labram HR Confocal, Horiba, France) (instrumental resolution ± 1 cm^{-1}) equipped with a 532 nm diode pumped solid state laser at 25 mW power. A field emission gun-scanning electron microscopy (FEG–SEM) (Sigma 500, Carl-Zeiss, Germany) was used to study the microstructure of the samples. Prior to electrical and ME measurements, silver paint was used on both surfaces of the pellets. The frequency dependent dielectric measurements (100 Hz–1 MHz) were carried out using impedance analyzer (Solarton I-1260, UK) at 40–400 °C. The composite specimens were poled for ferroelectric measurements at 10 kV with 2 cm tungsten needle to specimen distance using Corona poling unit (Millman thin films PVT. LTD. Pune, India). Keithley (6517B, USA) electrometer was used to measure the leakage current density (J) with varying *dc* electric field (E). The d_{33} measurements were carried out

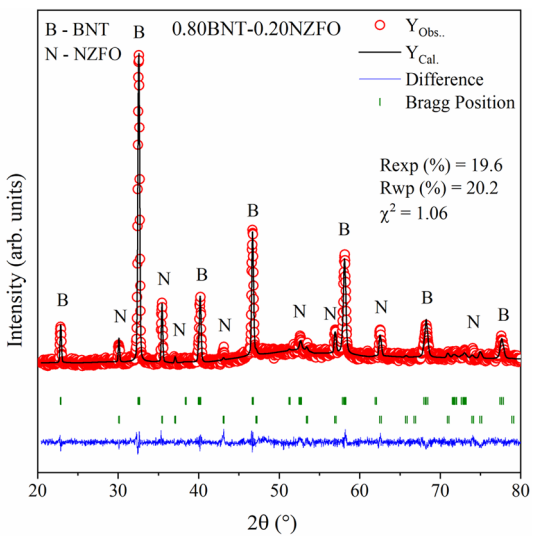

Fig. 1 Refined XRD pattern of 0.80BNT–0.20NZFO composite sintered at 1050 °C for 1 h

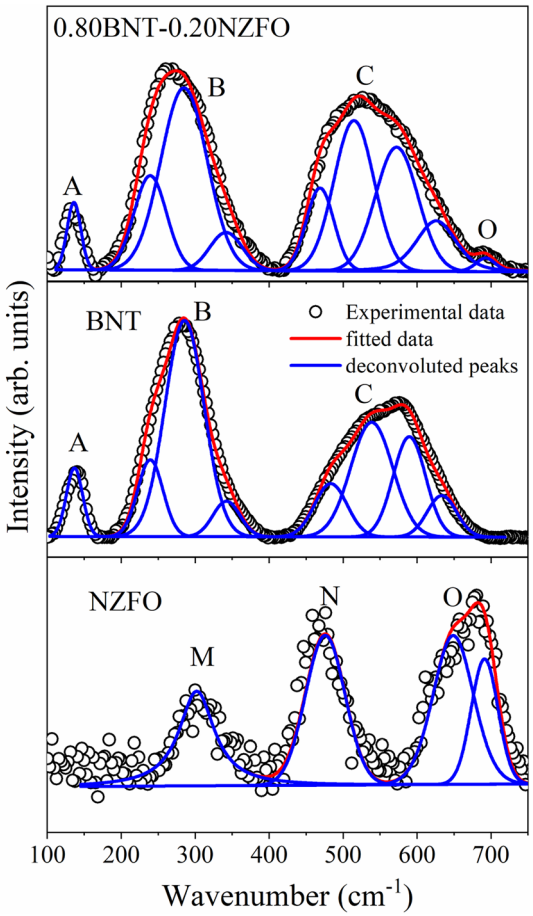

Fig. 2 Raman spectra of BNT, NZFO, and 0.80BNT–0.20NZFO ceramics

using d_{33} meter (Sinocera, YE2730A, China). Ferromagnetic studies were done by vibrating sample magnetometer (VSM) (Lakeshore-7404, USA). Further, the Precision multiferroic-II system (Radiant Technology, USA) was used for ferroelectric and *ME* voltage coefficient (α_{ME}) measurements. The *ME* measurements were carried out in an applied *ac* magnetic field of 3 Oe at 10 Hz using Helmholtz coil (Lakeshore MH-6, USA). The *dc* magnetic field was varied using electromagnets (GMW 5480, USA). In this charge (q) and capacitance (C) was measured with H_{dc} at fixed H_{ac}. The calculated voltage ($V_{out} = q/C$) was used to determine α_{ME} in terms of thickness (t) and H_{dc} as

$$\alpha_{ME} = \frac{V_{out}}{t.H_{dc}} \quad (1)$$

Table 1 Deconvoluted peak position of BNT and NZFO Raman spectra

Pure BNT		Pure NZFO	
Position (cm^{-1})	Bond	Position (cm^{-1})	Bond
137	Bi/Na–O	302	Zn/Fe–O
239	Ti–O	475	Zn/Fe–O
286	Ti–O	649	Ni/Fe–O
342	Ti–O	691	Ni/Fe–O
483	$Ti–O_6$	–	–
539	$Ti–O_6$	–	–
590	$Ti–O_6$	–	–
634	$Ti–O_6$	–	–

3 Results and Discussions

Figure 1 shows the representative XRD pattern of sintered 0.80BNT–0.20NZFO composite refined with rhombohedral (*R*3c) and cubic (*Fd*3*m*) phases. Both BNT and NZFO phases coexists without any impurity, which suggests no intermediate reaction has taken place among the phases within the used sintering conditions. The refined parameters, R_{exp}, R_{wp} were closed to 20 and χ^2 is nearly 1 that suggests good agreement between obtained and fitted patterns. No changes in the lattice parameters and characteristic peak positions were observed for both the phases with obvious reasons. The obtained phase fraction from the refinement is comparable with the relative weight fraction of individual phases that used to prepare composites.

Figure 2 depicts the Raman spectra of BNT, NZFO and 0.80BNT–0.20NZFO specimens ranging from 100 to 750 cm^{-1}. As suggested by group theory all 3 Raman active modes (A, B and C) are observed for BNT and in close agreement with previous studies [15, 17]. The bands A, B and C demonstrate the vibrations of Bi/Na–O, Ti–O, and $Ti–O_6$ octahedra respectively. Further, these bands were deconvoluted with eight peaks that expressed the stretching and bending of the metal–oxygen bonds. The spectra of NZFO showed three Raman bands denoted by M, N and O. The M and N are related to symmetric stretching and antisymmetric bending of metal–oxygen bonds at octahedral site respectively, whereas O corresponds to stretching at tetrahedral site [33]. The deconvoluted Raman peak positions of pure BNT and NZFO is tabulated in Table 1. In composites, the peaks of both the phases have been observed. However, low intensity of NZFO peaks ascribed to its low volume fraction. It is to be noted that similar to XRD, no change

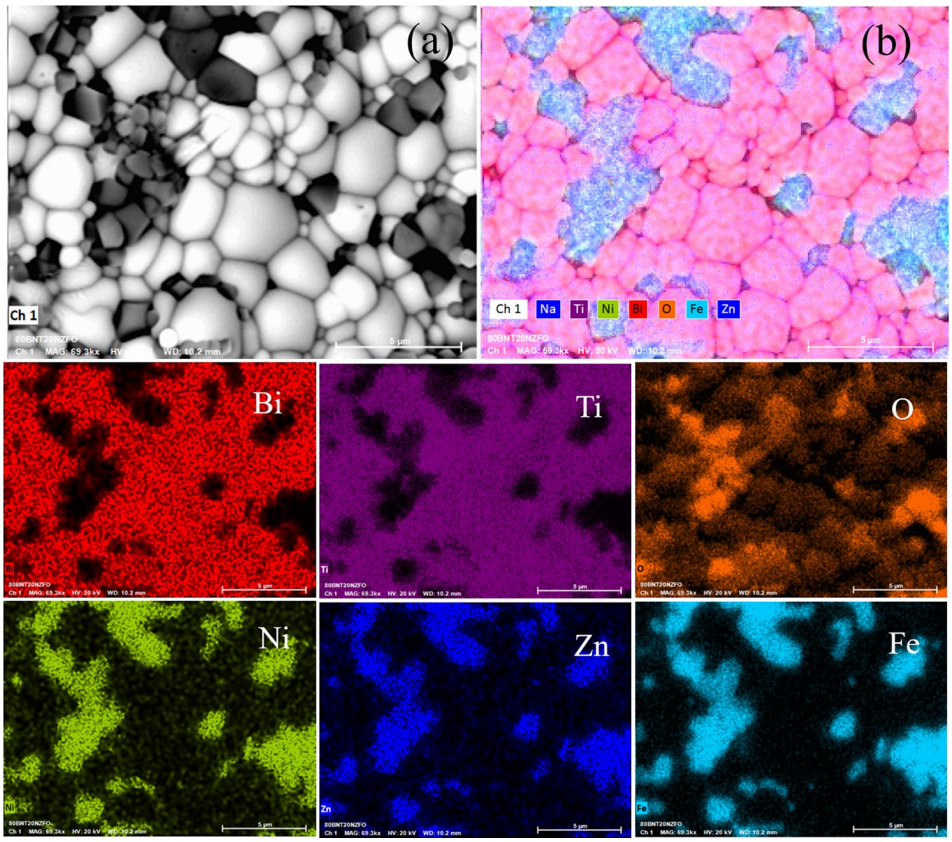

Fig. 3 Microstructure **a** backscattered image, **b** elemental color mapping of 0.80BNT–0.20NZFO ceramics

in peak position is observed, which denied the presence of micro-strain towards bond compression/stretching along interphase boundaries.

Figure 3 shows the representative backscattered electron images along with elemental mapping of 0.80BNT–0.20NZFO sintered composite. A dense microstructure with well distinguished sharp interphase boundaries of BNT (bright) and NZFO (dark) is clearly visible in the composite samples. Both phases have equiaxed grains with similar size distribution of 1–3 µm. However, the BNT shows larger fraction of coarse grains due to its higher phase fraction, whereas grain growth of NZFO may be hindered by the major BNT phase. The NZFO phase is found to be agglomerated as a consequence of mechanical mixing. The elemental mapping (Fig. 3b) along with individual elements present confirms BNT and NZFO grains as bright and dark contrast respectively in the samples. Mapping of Na element is beyond the detection limit of the equipment.

Figure 4 depicts the temperature (T) dependent dielectric constant (ε_r) and loss tangent (tanδ) at 1 MHz for (1−x)BNT–xNZFO specimens. For pure BNT and 0.90BNT–0.10NZFO specimens, ε_r found to increase gradually with temperature upto 220 °C and then a sharp increase has been observed. Previously, temperature dependent XRD and neutron diffraction studies suggested ferroelectric to anti-ferroelectric phase transition (referred as depolarization temperature, T_d), with a corresponding change in the crystal structure i.e., rhombohedral to tetragonal respectively [34, 35]. The enlarged view of tanδ for BNT (inset Fig. 4b) also confirmed the transition at 220 °C. The anomalous increase in ε_r upto 320 °C suggests that transition is not sharp and persists till 400 °C [36]. This increase in ε_r despite the occurrence of antiferroelectric phase, may be ascribed to the existence of interphase boundaries which contributes to the polarization. The decrease in ε_r above 320 °C (T_m) is due to antiferroelectric to paraelectric phase transition as supported by sharp increase in tanδ after 320 °C [36] The composite with higher NZFO ($x > 0.10$) content showed diffuse phase transition behavior, which is usually observed in ME composites [37, 38].

Figure 5 showed the frequency dependent conductivity (σ_{ac}) plots for BNT-NZFO specimens at different temperatures. The σ_{ac} is calculated by the formula [39, 40],

$$\sigma_{ac} = \varepsilon_0 \varepsilon'' \omega \quad (2)$$

here ε_0 is absolute permittivity in free space, ε'' is imaginary permittivity of specimen and $\omega = 2\pi f$ is angular frequency. The plot appears to be the combination of plateau and inclined conductivity regions. According to the Jonscher's

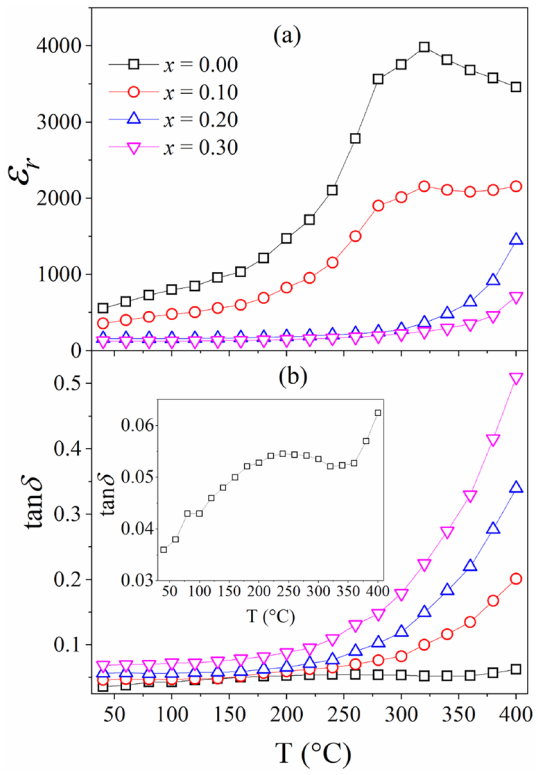

Fig. 4 Temperature dependent **a** ε_r and **b** tanδ of (1−x)BNT–xNZFO specimens at 1 MHz. Inset represent the enlarged view of tanδ for pure BNT

power law, the plateau indicates the *dc* conductivity (σ_{dc}) and inclined region represent frequency dependent conductivity ($A\omega^n$). Therefore, σ_{ac} can be written as [41]

$$\sigma_{ac} = \sigma_{dc} + A\omega^n \tag{3}$$

The increase in conductivity with frequency suggests that the conduction is governed by hopping of charge carriers between the localized state in accordance to Jump relaxation model (JRM) [42, 43]. On increasing temperature, thermally activated charge carriers contribute towards conduction. At sufficiently high temperatures, the contribution of frequency dependent conductivity is relatively small within the studied frequency range. Further Arrhenius plot of *dc* conductivity (σ_{dc}) for (1−x)BNT–xNZFO specimens are shown in Fig. 6. The activation energy (E_g) is calculated by

$$\sigma_{dc} = \sigma_0 \exp\left(-E_g/KT\right) \tag{4}$$

where K is the Boltzmann constant.

The conductivity increases with temperature for each specimen that represents their semiconducting behavior. Two slopes in low and high temperature regime are observed and suggests the different types of carriers are responsible for the conduction. At low temperatures, the conduction is governed by the hopping of electrons, while at high temperature the diffusion of oxygen vacancy contributes [44]. The increase in interphase boundaries fraction with NZFO content, restricts the movement of oxygen vacancies and consequently requires higher E_g as observed.

The ferroelectric behavior of (1−x)BNT–xNZFO specimens is confirmed by their *RT P–E* loops at 10 Hz as shown in Fig. 7a.

A well saturated hysteresis has been observed for $x = 0.00$ and $x = 0.05$. Further increase of low resistive NZFO phase enhances the conduction losses, result in low field sustainability and unsaturated loops of composites. The obvious decrease in P_r is found with non-ferroelectric NZFO phase induction as shown in Table 2. Figure 7b depicts the E dependent bipolar strain plot of BNT–NZFO specimens. A normalized strain of 105.2 pm/V has been observed in pure BNT, which is decreased in composites with NZFO content. Further, an obvious declined trend in d_{33} is observed with NZFO content as tabulated in Table 2. The enhancement of conduction losses with NZFO content in composite specimens is confirmed by *J–E* plots as shown in Fig. 7c. The sharp increase in J till 0.5 kV/cm attributes to the space charge conduction. Above 0.5 kV/cm, gradual increase of J indicates the contribution of grain boundaries, and Poole-Frankel emission [45, 46]. The *M–H* loops for (1−x)BNT–xNZFO specimens are shown in Fig. 7d. The saturation magnetization (M_s) increases in composites due to high magnetic phase (NZFO) content.

The *ME* coupling is a product tensor of both ferroelectric and ferromagnetic characteristics. As composite has exhibited both ferroelectric and ferromagnetic properties, a large *ME* response in such specimens is expected. The *ME* coefficient (α_{ME}) for all composites as a function of *dc* magnetic field (H_{dc}) with an *ac* field (H_{ac}) of 3 Oe at 10 Hz has shown in Fig. 8a. The α_{ME} increases with H_{dc} till 800 Oe and decreases afterward that suggest the maximum strain mediated coupling occurred at 800 Oe. As NZFO content increases α_{ME} also increases upto $x = 0.20$ content and thereafter decreases (Fig. 8b). The maximum obtained value of α_{ME} is 4.33 mV/cm.Oe for 0.80BNT–0.20NZFO composite. The low α_{ME} for composite below $x = 0.20$ is due to the small fraction of magnetostrictive phase. For $x > 0.20$, the lower value of α_{ME} is due to the excess amount of NZFO content that have high J and limits the poling effect in composite [47]. Further, the effect of f on α_{ME} has been investigated as shown in Fig. 8c. No noticeable changes have been observed with f

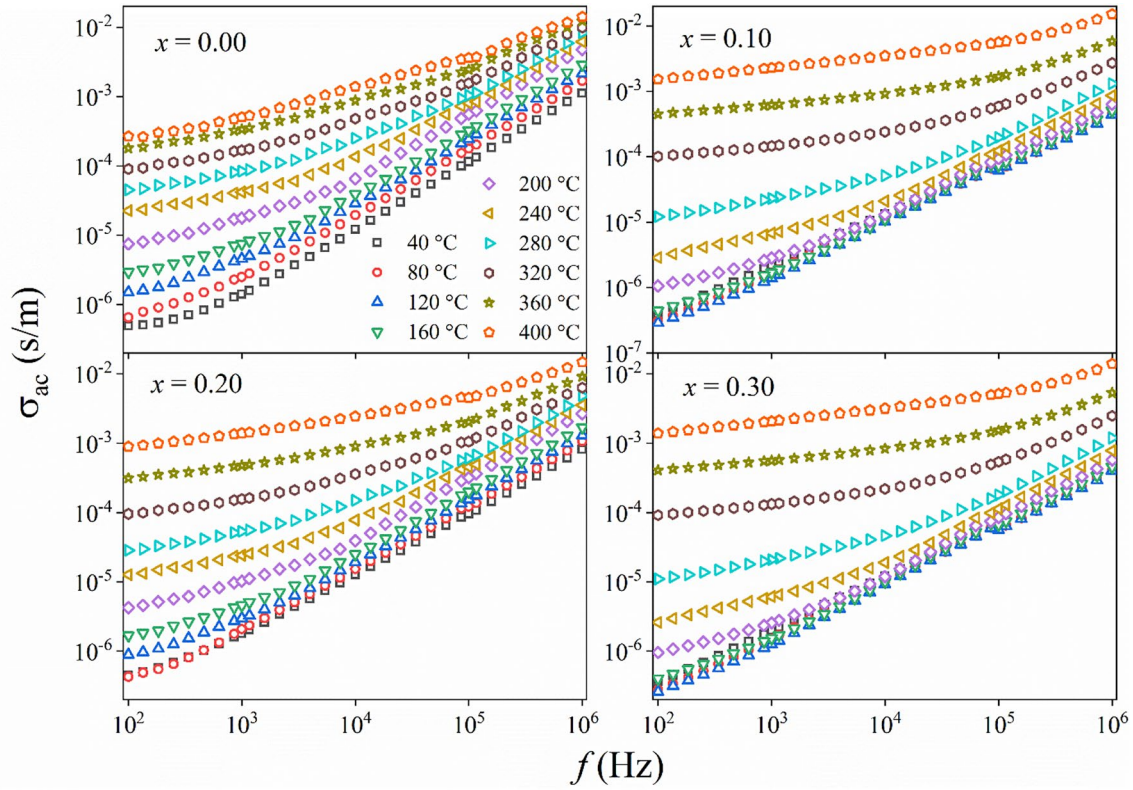

Fig. 5 Frequency dependent *ac* conductivity of (1−*x*) BNT–*x*NZFO specimens at different temperatures

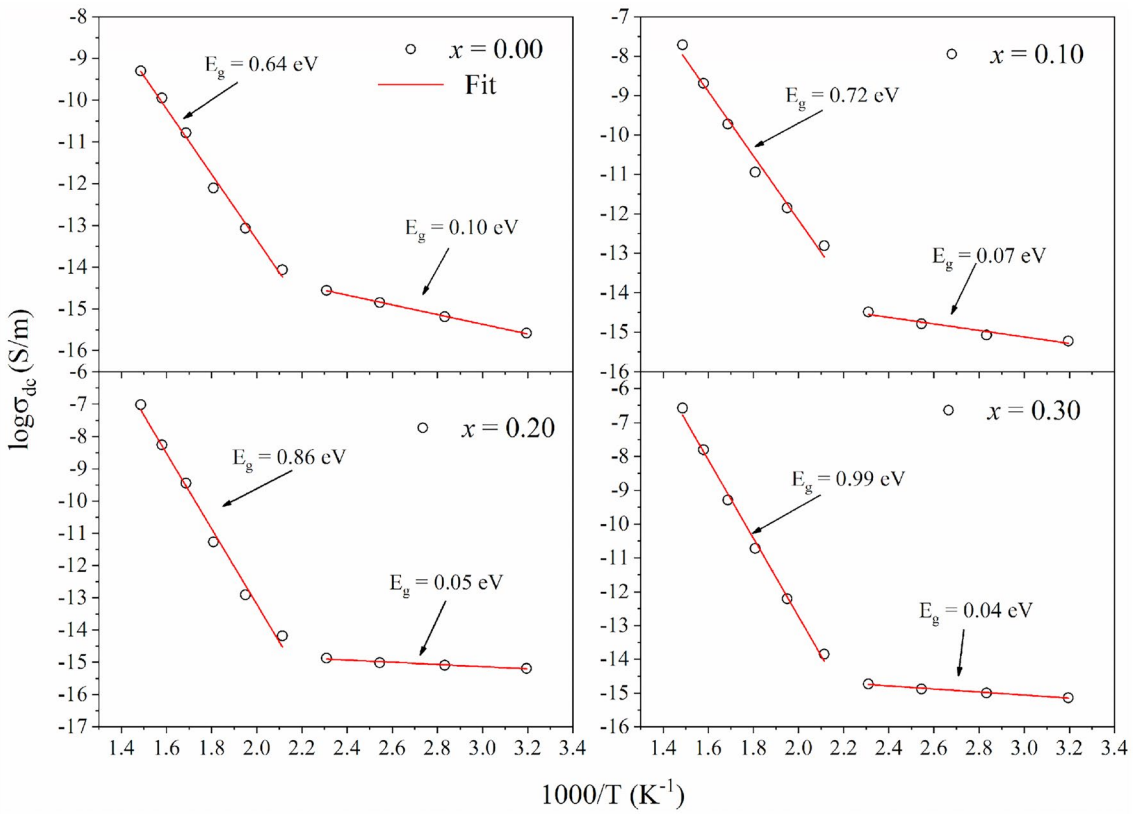

Fig. 6 Temperature dependent conductivity of (1−*x*)BNT–*x*NZFO specimens at 1 MHz

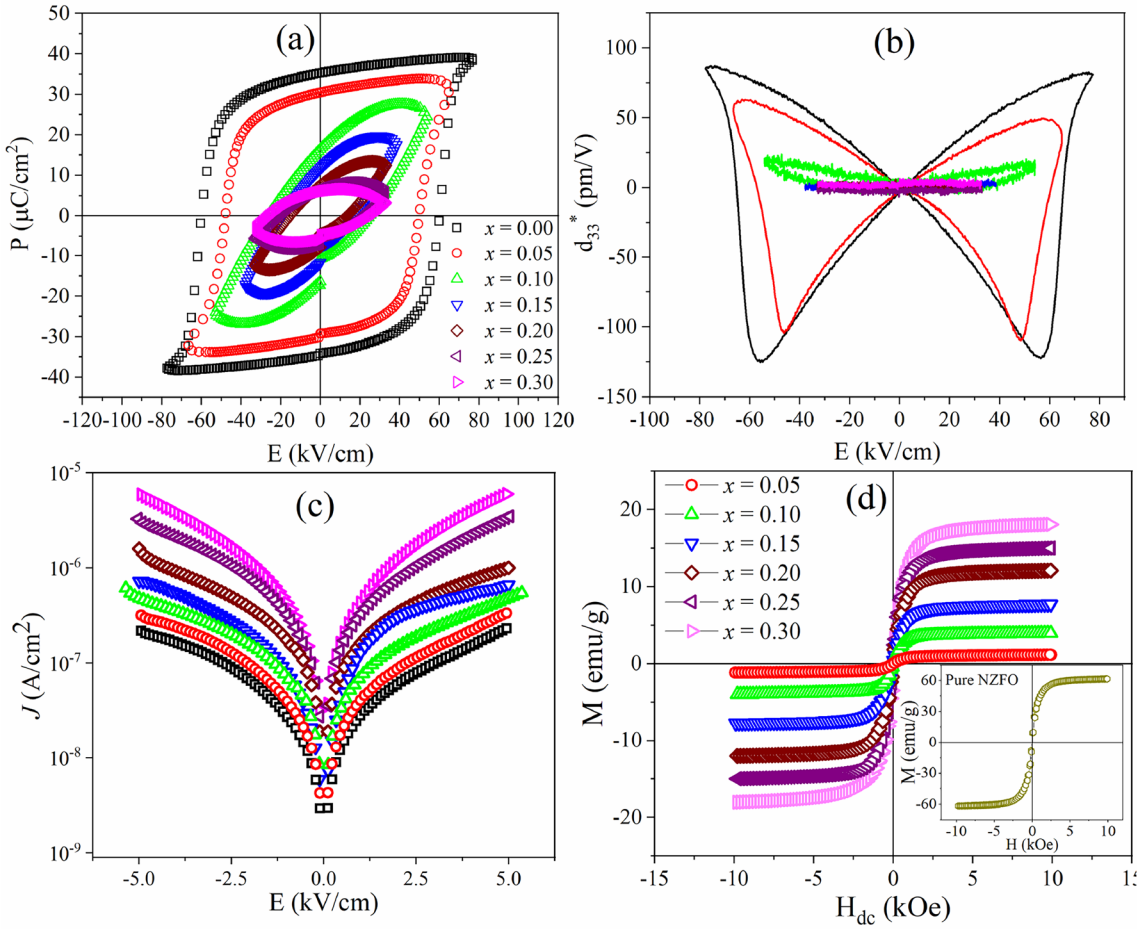

Fig. 7 **a** *P–E* loops, **b** d_{33}^*, **c** *J–E* measurements, and **d** *M–H* loops of (1−*x*)BNT–*x*NZFO specimens

Table 2 P_r, d_{33}, normalized d_{33}^*, *J*, and M_s of (1−*x*)BNT–*x*NZFO specimens

x	P_r (μC/cm²)	d_{33} (pC/N)	Normalized d_{33}^* (pm/V)	*J* (μA/cm²) at 5 kV/cm	M_s (emu/g)
0.00	35.35	47	105.2	0.23	–
0.05	30.48	36	83.7	0.34	1.16
0.10	16.62	25	20.3	0.55	3.97
0.15	11.76	19	5.6	0.67	7.71
0.20	7.61	15	4.1	0.94	12.07
0.25	6.70	11	3.4	3.49	15.02
0.30	6.04	7	2.9	5.98	18.13

that suggest the linear behavior of α_{ME} at off-resonance *f* condition [48, 49], which is further supported by identical behavior of α_{ME} for 0.8 BNT–0.2 NZFO with H_{dc} at different *f* as shown in Fig. 8d. The high value of α_{ME} at low frequency is not reported so far, which indicates the potential of material. A comparative of BNT based *ME* composites is shown in Table 3.

4 Conclusion

Lead-free *ME* particulate composite of BNT–NZFO were successfully synthesized. The coexistence of both phases was confirmed by XRD and FEG-SEM. The Raman spectroscopy suggested absence of interfacial micro-strains between BNT and NZFO phase. The temperature dependent dielectric study displayed the T_d (~ 220 °C) and T_m (~ 320 °C) for pristine BNT and 0.90BNT-0.10NZFO specimens. However, such transition temperatures were obscured in 0.80BNT–0.20NZFO and 0.70BNT–0.30NZFO. The frequency dependent σ_{ac} plot at different temperature followed the Jump relaxation model. The value of E_g was found to be increased with NZFO content that suggest the interphase boundaries restrict the movement of charge carriers. The NZFO content enhanced the ferroelectric losses and leakage current density in composites. An obvious increase in M_s with NZFO content were observed in composites. All samples showed good *ME* coupling and highest value of 4.33 mV/

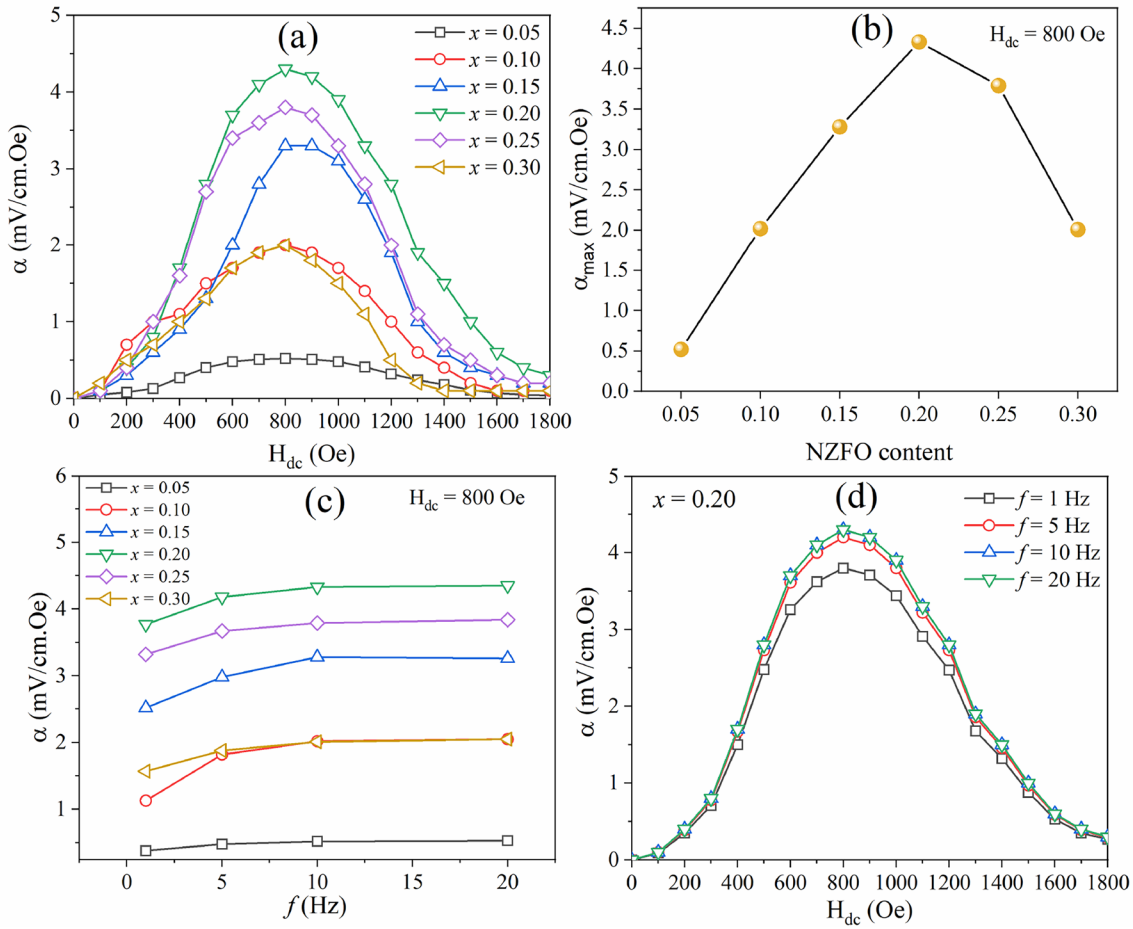

Fig. 8 Variation of α_{ME} with **a** H_{dc} at 10 Hz, **b** NZFO content and **c** f at 800 Oe for BNT–NZFO composites. **d** Variation in α_{ME} with H_{dc} at different f for 0.80BNT–0.20NZFO composite

Table 3 Comparison of *ME* coefficient at different frequency for BNT based composites

ME composite	Frequency (Hz)	ME coefficient (mv/cm.Oe)	References
$0.8Bi_{0.5}Na_{0.5}TiO_3$–$0.2MgFe_2O_4$	999	4.47	[30]
$0.6Bi_{0.5}Na_{0.5}TiO_3$–$0.4NiFe_2O_4$	847	1.12	[32]
$0.65Bi_{0.5}Na_{0.5}TiO_3$–$0.35CoFe_2O_4$	1000	0.50	[50]
$0.8Bi_{0.5}Na_{0.5}TiO_3$–$0.2Ni_{0.5}Zn_{0.5}Fe_2O_4$	10	4.33	This work

cm.Oe at 800 Oe was obtained for 0.80BNT–0.20NZFO at 10 Hz.

Acknowledgements The authors acknowledge DRDO, New Delhi for providing the grant through project (No. ERIP/ER/201709007/M/01/1731) to carry out this research. We are very thankful to DST (FIST-I & II) for providing VSM, FEG-SEM, Raman, and multiferroic measurement facility.

Declarations

Conflict of interest The authors declare that they have no known competing financial interests or personal relationships that could have appeared to influence the work reported in this paper.

References

1. Chu, Z., Pourhosseiniasl, M., Dong, S.: Review of multi-layered magnetoelectric composite materials and devices applications.

J. Phys. D Appl. Phys. **51**, 1–21 (2018). https://doi.org/10.1088/1361-6463/aac29b
2. Yu, S., Huang, H., Zhou, L., et al.: Structure and properties of PMN–PT/NZFO laminates and composites. Ceram. Int. **34**, 701–704 (2008). https://doi.org/10.1016/j.ceramint.2007.09.011
3. Rani, A., Kolte, J., Vadla, S.S., Gopalan, P.: Structural, electrical, magnetic and magnetoelectric properties of Fe doped $BaTiO_3$ ceramics. Ceram. Int. **42**, 8010–8016 (2016). https://doi.org/10.1016/j.ceramint.2016.01.205
4. Pradhan, D.K., Kumari, S., Rack, P.D.: Magnetoelectric composites: applications, coupling mechanisms, and future directions. Nanomaterials **10**, 1–22 (2020). https://doi.org/10.3390/nano10102072
5. Li, P., Wen, Y., Huang, X., et al.: Wide-bandwidth high-sensitivity magnetoelectric effect of magnetostrictive/piezoelectric composites under adjustable bias voltage. Sensors Actuators A Phys. **201**, 164–171 (2013). https://doi.org/10.1016/j.sna.2013.07.005
6. Zhou, Y., Apo, D.J., Priya, S.: Dual-phase self-biased magnetoelectric energy harvester. Appl. Phys. Lett. **103**, 1–5 (2013). https://doi.org/10.1063/1.4829151
7. Song, H., Hwang, G.-T., Ryu, J., Choi, H.: Stable output performance generated from a magneto-mechano-electric generator having self-resonance tunability with a movable proof mass. Nano Energy **101**, 107607 (2022). https://doi.org/10.1016/j.nanoen.2022.107607
8. Annapureddy, V., Palneedi, H., Hwang, G.T., et al.: Magnetic energy harvesting with magnetoelectrics: an emerging technology for self-powered autonomous systems. Sustain. Energy Fuels **1**, 2039–2052 (2017). https://doi.org/10.1039/c7se00403f
9. Pattanayak, R., Raut, S., Kuila, S., et al.: Multiferroism of [$Na_{0.5}Bi_{0.5}TiO_3$–$BaFe_{12}O_{19}$] lead-free novel composite systems. Mater. Lett. **209**, 280–283 (2017). https://doi.org/10.1016/j.matlet.2017.08.023
10. Fernandez Perdomo, C.P., Kiminami, A.R.H.G., Garcia, D.: Microwave assisted sintering of nanocristalline PMN–PT/$CoFe_2O_4$ prepared by rapid one pot pechini synthesis: dielectric and magnetoelectric characteristics. Ceram. Int. **45**, 7906–7915 (2019). https://doi.org/10.1016/j.ceramint.2019.01.101
11. Guo, R., Cross, L.E., Park, S.E., et al.: Origin of the high piezoelectric response in $PbZr_{1-x}Ti_xO_3$. Phys. Rev. Lett. **84**, 5423–5426 (2000). https://doi.org/10.1103/PhysRevLett.84.5423
12. Tyagi, M., Kumari, M., Chatterjee, R., Sharma, P.: Large magnetoelectric response in modified BNT based ternary piezoelectric [$72.5(Bi_{1/2}Na_{1/2}TiO_3$)–$22.5(Bi_{1/2}K_{1/2}TiO_3$)–$5(BiMg_{1/2}Ti_{1/2}O_3$)]-magnetostrictive ($NiFe_2O_4$) particulate (0–3) composites. Appl. Phys. Lett. **106**, 1–4 (2015). https://doi.org/10.1063/1.4921521
13. Ryu, J., Kang, J.E., Zhou, Y., et al.: Ubiquitous magneto-mechano-electric generator. Energy Environ. Sci. **8**, 2402–2408 (2015). https://doi.org/10.1039/c5ee00414d
14. Annapureddy, V., Na, S.M., Hwang, G.T., et al.: Exceeding milliwatt powering magneto-mechano-electric generator for standalone-powered electronics. Energy Environ. Sci. **11**, 818–829 (2018). https://doi.org/10.1039/c7ee03429f
15. Song, H., Patil, D.R., Yoon, W.H., et al.: Significant power enhancement of magneto-mechano-electric generators by magnetic flux concentration. Energy Environ. Sci. **13**, 4238–4248 (2020). https://doi.org/10.1039/d0ee01574a
16. Venkata Ramana, E., Zavašnik, J., Graça, M.P.F., Valente, M.A.: Magnetoelectric studies on $CoFe_2O_4$/0.5($BaTi_{0.8}Zr_{0.2}O_3$)-0.5($Ba_{0.7}Ca_{0.3}TiO_3$) lead-free bilayer thin films derived by the chemical solution deposition. J. Appl. Phys. **120**, 1–10 (2016). https://doi.org/10.1063/1.4961394
17. Shrout, T.R., Zhang, S.J.: Lead-free piezoelectric ceramics: Alternatives for PZT? J. Electroceram. **19**, 111–124 (2007). https://doi.org/10.1007/s10832-007-9047-0
18. Saito, Y., Takao, H., Tani, T., et al.: Lead-free piezoceramics. Nature **432**, 84–87 (2004). https://doi.org/10.1038/nature03028
19. Singh, P., Laishram, R., Sharma, P., Kolte, J.: Giant magnetocapacitance in magnetoelectric BNT/NFO particulate composites. J. Mater. Sci. Mater. Electron. **32**, 21288–21296 (2021). https://doi.org/10.1007/s10854-021-06631-w
20. Niranjan, M.K., Karthik, T., Asthana, S., et al.: Theoretical and experimental investigation of Raman modes, ferroelectric and dielectric properties of relaxor $Na_{0.5}Bi_{0.5}TiO_3$. J. Appl. Phys. **113**, 1–7 (2013). https://doi.org/10.1063/1.4804940
21. Karthik, T., Asthana, S.: Polarization extension mechanism revealed through dynamic ferroelectric hysteresis and electric field driven structural distortions in lead free $Na_{0.5}Bi_{0.5}TiO_3$ ceramic. J. Phys. D Appl. Phys. **50**, 1–6 (2017). https://doi.org/10.1088/1361-6463/aa7fa7
22. Sahu, M., Karthik, T., Srinivas, A., Asthana, S.: Structural and microstructural correlation with ferroelectric and dielectric properties of nanostructured $Na_{0.5}Bi_{0.5}TiO_3$ ceramics. J. Mater. Sci. Mater. Electron. **26**, 9741–9746 (2015). https://doi.org/10.1007/s10854-015-3643-6
23. Narendra Babu, S., Hsu, J.H., Chen, Y.S., Lin, J.G.: Magnetoelectric response in lead-free multiferroic $NiFe_2O_4$–$Na_{0.5}Bi_{0.5}TiO_3$ composites. J. Appl. Phys. **109**, 1–3 (2011). https://doi.org/10.1063/1.3540623
24. Bichurin, M., Petrov, V., Zakharov, A., et al.: Magnetoelectric interactions in lead-based and lead-free composites. Materials (Basel) **4**, 651–702 (2010). https://doi.org/10.3390/ma4040651
25. Jaffe, H.: Piezoelectric ceramics. J. Am. Ceram. Soc. **41**, 494–498 (1958). https://doi.org/10.1111/j.1151-2916.1958.tb12903.x
26. Costa, A.C.F.M., Silva, V.J., Cornejo, D.R., et al.: Magnetic and structural properties of $NiFe_2O_4$ ferrite nanopowder doped with Zn^{2+}. J. Magn. Magn. Mater. **320**, 370–372 (2008). https://doi.org/10.1016/j.jmmm.2008.02.159
27. Zhang, Y.Z., Kang, Z.T., Chen, D.: Process of synthesizing high saturation magnetization $Ni_{0.5}Zn_{0.5}Fe_2O_4$ by microwave assisted ball milling. Mater. Lett. **133**, 259–261 (2014). https://doi.org/10.1016/j.matlet.2014.07.031
28. Atif, M., Nadeem, M., Grössinger, R., Turtelli, R.S.: Studies on the magnetic, magnetostrictive and electrical properties of sol–gel synthesized Zn doped nickel ferrite. J. Alloys Compd. **509**, 5720–5724 (2011). https://doi.org/10.1016/j.jallcom.2011.02.163
29. Kumar, Y., Yadav, K.L., Manjusha, J., et al.: Structural, dielectric, magnetic and magnetoelectric properties of (x)$Bi_{0.5}Na_{0.5}TiO_3$–(1–x)$Ni_{0.2}Co_{0.8}Fe_2O_4$ composites. Mater. Res. Exp. **3**, 1–9 (2016). https://doi.org/10.1088/2053-1591/3/6/065701
30. Manjusha, Yadav KL., Adhlakha, N., et al.: Strain mediated magnetoelectric coupling induced in (x)$Bi_{0.5}Na_{0.5}TiO_3$–(1–x)$MgFe_2O_4$ composites. Phys. B Condens. Matter. **514**, 41–50 (2017). https://doi.org/10.1016/j.physb.2017.03.027
31. Kumar, Y., Yadav, K.L., Shah, J., Kotnala, R.K.: Investigation of magnetoelectric effect in $Bi_{0.5}Na_{0.5}TiO_3$–$CoMn_{0.2}Fe_{1.8}O_4$ composites. IEEE Trans. Dielectr. Electr. Insul. **26**, 561–567 (2019). https://doi.org/10.1109/TDEI.2019.007577
32. Bhasin, T., Agarwal, A., Sanghi, S., et al.: Crystal structure, dielectric, magnetic and improved magnetoelectric properties of x$NiFe_2O_4$–(1–x)$Na_{0.5}Bi_{0.5}TiO_3$ composites. Mater. Res. Exp. **5**, 1–15 (2018). https://doi.org/10.1088/2053-1591/aad9e3
33. Jadhav, J., Biswas, S., Yadav, A.K., et al.: Structural and magnetic properties of nanocrystalline Ni–Zn ferrites: in the context of cationic distribution. J. Alloys Compd. **696**, 28–41 (2017). https://doi.org/10.1016/j.jallcom.2016.11.163
34. Xu, C., Lin, D., Kwok, K.W.: Structure, electrical properties and depolarization temperature of ($Bi_{0.5}Na_{0.5}$)TiO_3–$BaTiO_3$ lead-free piezoelectric ceramics. Solid State Sci. **10**, 934–940 (2008). https://doi.org/10.1016/j.solidstatesciences.2007.11.003

35. Tan, X., Ma, C., Frederick, J., et al.: The antiferroelectric ↔ ferroelectric phase transition in lead-containing and lead-free perovskite ceramics. J. Am. Ceram. Soc. **94**, 4091–4107 (2011). https://doi.org/10.1111/j.1551-2916.2011.04917.x
36. Jones, G., Thomas, P.A.: Investigation of the structure and phase transitions in the novel A-site substituted distorted perovskite compound $Na_{0.5}Bi_{0.5}TiO_3$. Acta Crystallogr. Sect. B **58**, 168–178 (2002)
37. Ciomaga, C.E., Neagu, A.M., Pop, M.V., et al.: Ferroelectric and dielectric properties of ferrite-ferroelectric ceramic composites. J Appl Phys **113**, 1–8 (2013). https://doi.org/10.1063/1.4792494
38. Rathore, S.S., Vitta, S.: Large low field room temperature magneto-dielectric response from $(Sr_{0.5}Ba_{0.5})Nb_2O_6/Co(Cr_{0.4}Fe_{1.6})O_4$ bulk 3–0 composites. Mater. Sci. Eng. B Solid-State Mater. Adv. Technol. **204**, 1–7 (2016). https://doi.org/10.1016/j.mseb.2015.11.002
39. Elliott, S.R.: A.c. conduction in amorphous chalcogenide and pnictide semiconductors. Adv. Phys. **36**, 135–217 (1987). https://doi.org/10.1080/00018738700101971
40. Long, A.R.: Frequency-dependent loss in amorphous semiconductors. Adv. Phys. **31**, 553–637 (1982)
41. Jonscher, A.K.: Review a new understanding of the dielectric relaxation of solids. J. Mater. Sci. **16**, 2037–2060 (1981)
42. Solid, P.S., Chem, S.: Jump relaxation in solid electrolytes. Prog. Solid State Chem. **22**, 111–195 (1993)
43. Sharma, R., Pahuja, P., Tandon, R.P.: Structural, dielectric, ferromagnetic, ferroelectric and *ac* conductivity studies of the $BaTiO_3$-$CoFe_{1.8}Zn_{0.2}O_4$ multiferroic particulate composites. Ceram. Int. **40**, 9027–9036 (2014). https://doi.org/10.1016/j.ceramint.2014.01.115
44. Tirupathi, P., Mandal, S.K., Chandra, A.: Effect of oxygen annealing on the multiferroic properties of Ca^{2+} doped $BiFeO_3$ nanoceramics. J. Appl. Phys. **116**, 1–14 (2014). https://doi.org/10.1063/1.4904861
45. Dietz, G.W., Antpöhler, W., Klee, M., Waser, R.: Electrode influence on the charge transport through $SrTiO_3$ thin films. J. Appl. Phys. **78**, 6113–6121 (1995). https://doi.org/10.1063/1.360553
46. Li, G., Wu, X., Ren, W., Shi, P.: Effect of excessive K and Na on the dielectric properties of (K, Na)NbO_3 thin films. Thin Solid Films **548**, 556–559 (2013). https://doi.org/10.1016/j.tsf.2013.09.027
47. Ryu, J., Priya, S., Uchino, K., Kim, H.: Magnetoelectric effect in composites of magnetostrictive and piezoelectric materials. J Electroceram. **8**, 107–119 (2002). https://doi.org/10.1023/A:1020599728432
48. Kang, M.G., Sriramdas, R., Lee, H., et al.: High power magnetic field energy harvesting through amplified magneto-mechanical vibration. Adv. Energy Mater. **8**, 1–11 (2018). https://doi.org/10.1002/aenm.201703313
49. Annapureddy, V., Kim, M., Palneedi, H., et al.: Low-loss piezoelectric single-crystal fibers for enhanced magnetic energy harvesting with magnetoelectric composite. Adv. Energy Mater. **6**, 1–10 (2016). https://doi.org/10.1002/aenm.201601244
50. Krishnaiah, R.V., Srinivas, A., Kamat, S.V., et al.: Effect of $CoFe_2O_4$ mole percentage on multiferroic and magnetoelectric properties of $Na_{0.5}Bi_{0.5}TiO_3/CoFe_2O_4$ particulate composites. Ceram. Int. **40**, 7799–7804 (2014). https://doi.org/10.1016/j.ceramint.2013.12.123